

# Collapse analysis of wind turbine tower under the coupled effects of wind and near-field earthquake

Jian Fan<sup>1</sup> | Qian Li<sup>1</sup> | Yanping Zhang<sup>2</sup>

<sup>1</sup>School of Civil Engineering and Mechanics, Huazhong University of Science and Technology, Wuhan, China

<sup>2</sup>School of Energy and Power Engineering, Huazhong University of Science and Technology, Wuhan, China

## Correspondence

Yanping Zhang, School of Energy and Power Engineering, Huazhong University of Science and Technology, Wuhan 430074, China.  
Email: zyp2817@mail.hust.edu.cn

## Abstract

In this paper, the pattern of wind turbine tower collapse as a result of the coupled effects of wind and an intense, near-field earthquake is investigated. The constitutive relation of the tower cylinder steel is simulated via a nonlinear kinematic hardening model, and the specific value of each parameter in the constitutive model is provided. A precise model of the tower structure coupled with the blade is created using a nonlinear, finite element method. This method is compared with the results from a static pushover test of a small cylindrical tower to validate the finite element modeling method in this research. Two earthquake wave sets are selected as inputs. One contains 20 near-field velocity pulse-like ground motion waves with various pulse periods; the other contains 20 ordinary far-field ground motion waves. A wind turbine tower with a hub height of 60 m is selected as an example for analysis. The dynamic response of this tower as a result of the coupled effects of the two ground motion wave sets and a transient wind load is calculated using nonlinear time-history analysis. The calculation results shows that the average horizontal displacement of the tower top as a result of the near-field velocity pulse-like ground motion is 33% larger than the case with far-field ground motion. Finally, the seismic collapse vulnerability curve of this wind turbine tower is calculated. The seismic collapse capacity of the tower is evaluated, and the seismic collapse pattern of the tower is analyzed.

## KEYWORDS

collapse, dynamic response, near-field earthquake, wind load, wind turbine tower

## 1 | INTRODUCTION

With the development of the wind energy industry, an increasing number of wind farms have been constructed in active earthquake zones. It is worth noting that, some wind-energy-rich regions are vulnerable to high-intensity earthquakes. An example is the pan-Pacific Ocean region, including the west coast of the United States and the east coast in Asia. In addition, the southeast coast of China is in this region. Wind farms in these regions may also be in potential earthquake fault zones and are vulnerable to near-field velocity pulse-like earthquakes. Therefore, the earthquake load becomes an important factor in wind turbine tower design.

In recent decades, many researchers have analyzed the earthquake response of wind turbines using popular computation software systems such as GH Bladed developed by Garrad Hassan<sup>1</sup> and FAST by NREL.<sup>2</sup> These two computation software systems are employed to simulate the dynamic response of a wind turbine based on multisystem dynamics and elastic body modal analysis. In the early days, using Bladed software, Witcher<sup>3</sup> created an earthquake analysis model for a 2-MW steel cylinder wind turbine and investigated the response of the wind turbine tower under three load conditions including stop, operation, and earthquake-induced emergent stop. More recently, Sanfangelo<sup>4</sup> modeled an entire NREL 5-MW wind turbine system using Bladed software and investigated the precision of the wind and earthquake using a noncoupled analysis method. Prowell et al<sup>5,6</sup> simulated the dynamic response of a 5-MW wind turbine subjected to an earthquake via FAST and suggested that the

bending moment at tower base in response to an earthquake in a high-intensity region was the internal control force in wind turbine tower design. Although multisystem dynamics and modal analysis have been combined to analyze the dynamic response of wind turbines, an approach, which has developed significantly in recent years,<sup>7-13</sup> such a method is unable to simulate the nonlinear behavior of the tower structure material and cannot precisely simulate wind turbine failure and collapse under extreme loading conditions.

With the development of computation tools, the nonlinear finite element method has become an important tool to calculate the earthquake response of a wind turbine tower. In the early days, Bazeos<sup>14</sup> and Lavassas<sup>15</sup> simulated a tower cylinder via a shell element and the cabin and blade combination with a mass concentrated at the top of the tower and calculated earthquake responses of two wind turbines (450 kW and 1 MW) in Greece. As the nonlinear finite element method considers the effect of material and geometrical nonlinearity on structure dynamic response, this method can accurately forecast various types of damage to a wind turbine tower. In recent years, under the framework of probability analysis, some researchers have investigated the earthquake vulnerability of wind turbine towers via nonlinear finite element methods. Nuta et al<sup>16</sup> performed increment dynamic analysis (IDA) for a 1.65-MW wind turbine tower using Ansys and calculated the earthquake vulnerability curve of this tower. Earthquake waves including actual earthquake records in Los Angeles and west Canada were used, and the effects of factors such as different ground motion intensity parameters, structure damage indexes, and damage levels on the earthquake vulnerability of a tower were investigated. Asareh et al<sup>17-19</sup> investigated earthquake vulnerability of a 5-MW wind turbine tower subject to the coupled effect of wind and earthquake using ABAQUS finite element software and considered the effect of average wind velocity. The results showed that the impact of wind load on the earthquake vulnerability of a wind turbine tower was insignificant. Patil et al<sup>20</sup> created a nonlinear finite element model for an 80-m high wind turbine tower using ABAQUS software and investigated the seismic performance of this tower via earthquake vulnerability analysis. Research showed that when subjected to an earthquake, this tower was most likely to develop an overturning failure, which was followed by tower base material yield and then permanent deformation and global instability. Kim et al<sup>21</sup> considered the interaction of the soil-pile structure and performed earthquake vulnerability analysis for a 5-MW offshore wind turbine tower; yield stress, yield displacement, and allowed displacement were used as damage parameters to calculate the structure's failure probability. Recently, Mo et al<sup>22</sup> created a model for a single pile offshore wind turbine tower using the OpenSees finite element platform and simulated the steel cylinder of the tower body by a nonlinear fiber beam element. This research also considered the interaction of the soil-pile structure and the effects of factors such as wind load and wave load and calculated the earthquake vulnerability curve of this tower using truncated increment dynamic analysis (TIDA).

The mass of a wind turbine tower structure is primarily concentrated at the tower top, which is a typical high-rise structure with a large natural vibration period. Some wind farms are near potential earthquake fault zones, and wind turbines in these wind farms are vulnerable to near-field pulse-like ground motion. Near-field pulse-like ground motion has a pulse-like waveform, a large velocity peak, a long pulse period, and rich medium and long period components. Research showed that under this type of ground motion, a structure with medium and long periods may cause serious damage.<sup>23-25</sup> In recent years, some researchers have investigated the dynamic response of a wind turbine tower under near-field ground motion. Stamatopoulos<sup>26</sup> investigated the earthquake response pattern of a wind turbine near earthquake fault zones in Greece. Research showed that base shear force and overturning bending moment calculated via time-history analysis was larger than these results from elastic reaction spectrum analysis (specifically, the elastic acceleration reaction spectrum in the near-field zone increased by 25%). Therefore, in Greek antiseismic specifications, the elastic acceleration reaction spectrum in near-field zones requires further improvement. Sadowski et al<sup>27</sup> investigated the dynamic response pattern of a wind turbine tower with a cylinder with an initial defect subjected to near-field and far-field ground motion. For the near-field pulse ground motion, the tower damage was much more severe than the damage from far-field ground motion. In a recent review article, Katsanos et al<sup>28</sup> mentioned that the effect of near-field ground motion on wind turbine towers should be investigated further.

The previously mentioned research shows that although some researchers have analyzed the earthquake response of wind turbine towers using nonlinear finite element software, the constitutive material relation in those studies was relatively simple, and studies on the collapse pattern of wind turbine towers subject to intense ground motion are scarce. In this paper, based on the ABAQUS finite element platform, the constitutive relation of the tower steel cylinder is simulated using a nonlinear kinematic hardening model; the dynamic response of the wind turbine tower subject to the coupled effects of wind and near-field pulse ground motion is calculated, and the effect of the pulse period on the earthquake response of a tower is investigated. Finally, the collapse capacity and collapse pattern of a wind turbine tower subject to an intense near-field earthquake is investigated.

## 2 | CREATION OF THE FINITE ELEMENT MODEL

### 2.1 | Element selection

When creating the finite element model for wind turbine tower, to reduce workload, some auxiliary structures with minor impact are ignored to simplify complex parts without affecting the dynamic characteristics of the wind turbine tower structure. The wind turbine tower is normally a thin-walled cylinder. On the basis of geometrical and stress characteristics, it is simplified as a shell element for processing. The weight of the cabin and hub is applied to the tower top as a concentrated point of mass, and the effect of its shape on the structure is ignored. Because the wind turbine blade is a slender bar with variable cross-section, it is simplified as a segmented elastic beam element for processing. To model the

interaction between the blade and the tower, these two elements are connected using a beam element with a large stiffness. The cabin and hub are simulated using concentrated mass elements and are placed at the tower top and blade connection center. The wind turbine tower base is normally connected to the foundation via bolts. To simplify modeling, the base is fixed; ie, all degrees of freedom are constrained. The finite element model for the wind turbine tower is shown in Figure 1.

## 2.2 | Constitutive relation of the material

In this paper, the constitutive relation of the steel tower cylinder is simulated via a nonlinear kinematic hardening model. The loading surface of this model has both uniform expansion and translation, which effectively simulates the strengthening effect and the Bauschinger effect during the material loading process. The equivalent yield surface of this model is defined as follows:

$$F(\sigma) = \left[ \frac{3}{2} (\mathbf{S} - \boldsymbol{\alpha}^{dev}) : (\mathbf{S} - \boldsymbol{\alpha}^{dev}) \right]^{1/2} - \sigma_0 = 0, \quad (1)$$

where  $\sigma$  is stress tensor,  $\mathbf{S}$  is deviatoric stress tensor,  $\boldsymbol{\alpha}^{dev}$  is deviatoric back stress tensor, and  $\sigma_0$  is hardening yield stress.

Assume that the corresponding plasticity flow law is

$$\dot{\boldsymbol{\epsilon}}^{pl} = \frac{\partial F(\sigma)}{\partial \sigma} \dot{\bar{\boldsymbol{\epsilon}}}^{pl}, \quad (2)$$

where  $\dot{\boldsymbol{\epsilon}}^{pl}$  is plastic strain rate and  $\dot{\bar{\boldsymbol{\epsilon}}}^{pl}$  represents the equivalent plastic strain rate.

Under cyclic loading, the material strengthening rule is shown in Figure 2. The kinematic hardening component adds a slack variable to the Ziegler strengthening rule. Additionally, the effect of multiple back stress is considered. The incremental form of back stress is as follows:

$$\dot{\boldsymbol{\alpha}}_k = C_k \frac{1}{\sigma_0} (\sigma - \boldsymbol{\alpha}) \dot{\bar{\boldsymbol{\epsilon}}}^{pl} - \gamma_k \boldsymbol{\alpha}_k \dot{\bar{\boldsymbol{\epsilon}}}^{pl}, \quad (3)$$

where  $C_k$  and  $\gamma_k$  are material parameters.  $C_k$  is the initial kinematic hardening modulus. In the  $\sigma - \bar{\boldsymbol{\epsilon}}^{pl}$  curve, it represents the tangential slope of the curve at the initial point.  $\gamma_k$  represents the reduction ratio of the kinematic hardening modulus versus the increase of plastic deformation. When  $\gamma_k = 0$ , the model degrades into the isotropic hardening model. The sum of the back stress  $\boldsymbol{\alpha}$  is calculated using the following formula:

$$\boldsymbol{\alpha} = \sum_{k=1}^N \boldsymbol{\alpha}_k, \quad (4)$$

where  $N$  is the number of back stresses.

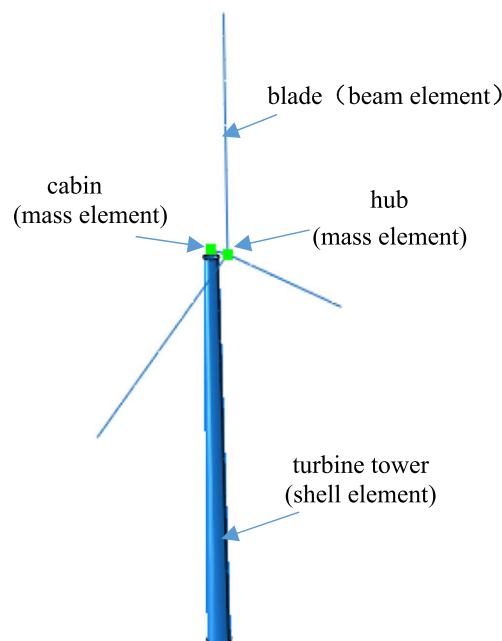


**FIGURE 1** Wind turbine tower finite element model [Colour figure can be viewed at [wileyonlinelibrary.com](http://wileyonlinelibrary.com)]

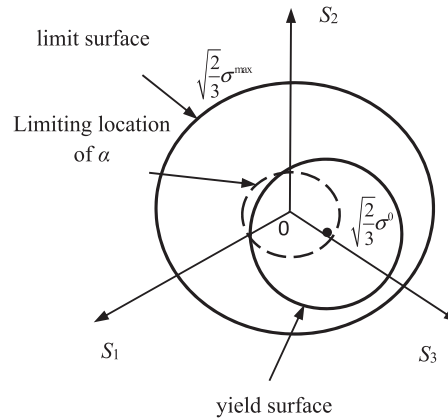


**FIGURE 2** Hardening criteria for the material

The strengthening yield stress  $\sigma^0$  is defined as the function of equivalent plastic strain  $\bar{\epsilon}^{pl}$ .

$$\sigma^0 = \sigma^0(\bar{\epsilon}^{pl}) = \sigma|_0 + Q_\infty(1 - e^{-b\bar{\epsilon}^{pl}}), \quad (5)$$

where  $\sigma|_0$  represents the yield stress under zero plastic strain and  $Q_\infty$  and  $b$  are material parameters.  $Q_\infty$  represents the maximum variation of the yield surface;  $b$  represents the variation ratio of the yield surface versus the plastic strain.

In the model, the value of each parameter is determined based on the following principle:

Under zero plastic strain, the yield stress is  $\sigma|_0 = 0.85 f_y$ , where  $f_y$  is the material yield strength.

The initial kinematic hardening modulus is  $C = 0.02E$ , and  $E$  is the material elastic modulus.

The reduction ratio of the kinematic hardening modulus versus the increase of plastic deformation is  $\gamma = C/[(f_{yu} - \sigma_0)M]$ ;  $M$  is the kinematic hardening proportion parameter, 0.5;  $f_{yu}$  is the ultimate strength of the material.

The maximum variation of the yield surface is  $Q_\infty = (f_{yu} - \sigma_0)$ .

The variation ratio of the yield surface is  $b = 0.5C/Q_\infty$ .

### 2.3 | Verification of the finite element model

In 2010, the University of California performed a static test for a 21.9-m high small wind turbine tower cylinder, which consisted of five parts. For detailed dimensions, please refer to a previous study.<sup>29</sup> The tower material is steel with an elastic modulus of 210 GPa, a Poisson ratio of 0.3, and a yield intensity of 270 MPa. During the test, the tower base was fixed. A displacement load was applied to the tower top gradually to create tower deformation. The tower base shear force and tower top displacement were measured (Figure 3A).

To validate the finite element modeling method, a finite element model for this tower cylinder is created using ABAQUS (Figure 3B). The model base is fixed, and a displacement load is applied to tower top. The tower base shear force is extracted to create a relation curve between base shear force and top displacement (see the “Numerical result 1” in Figure 3A). Figure 3A shows that when the tower top displacement is small, the tower base shear force changes linearly with tower top displacement. When the displacement increases to 0.2 m, the tower midsection starts

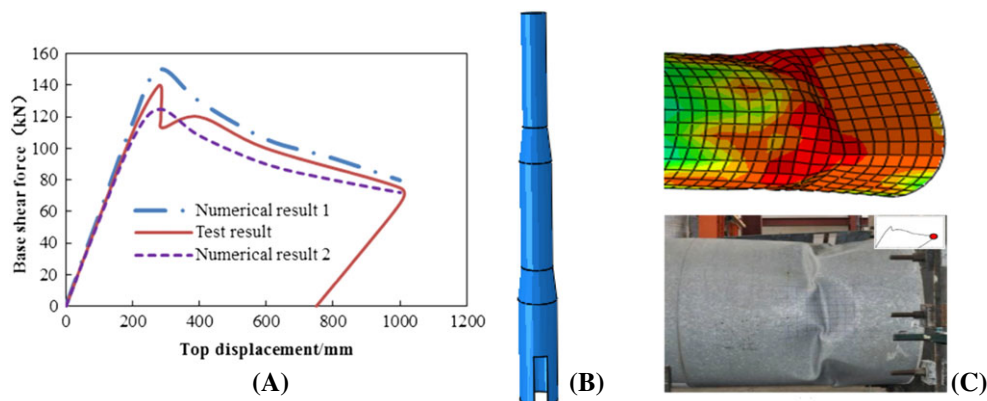


**FIGURE 3** Finite element model verification, A, relation curve between base shear force and top displacement, B, tower cylinder finite element model, C, local deformation comparison diagram [Colour figure can be viewed at [wileyonlinelibrary.com](http://wileyonlinelibrary.com)]

to yield. When displacement reaches 0.3 m, the tower cylinder midsection yield reaches its maximum level. At this moment, the base shear force is 155 kN. As displacement continues to increase, the base shear force decreases. In order to compare the influence of constitutive models on numerical results, the relation curve between base shear force and top displacement is calculated by simple elastic-plastic constitutive model (see the "Numerical result 2" in Figure 3A). Comparing with the testing results, it could be concluded that the "Numerical result 2" will underestimate the horizontal ultimate bearing capacity of tower tube and has a slightly larger error than "Numerical result 1." Figure 3C shows the local deformation comparison diagram when the tower cylinder failure occurs. The diagram shows that the ABAQUS finite element model calculation result matches the test result, which verifies the finite element modeling method.

### 3 | WIND LOAD FORMATION AND EARTHQUAKE WAVE SELECTION

#### 3.1 | Wind load formation

When the wind passes the wind turbine blades, lift and drag forces are generated. Lift rotates the blade, and drag results in the vibration of the blade and the tower along the wind direction. This paper only considers the effect of drag. The formula for calculating the wind load on the tower and the blade at a given time is as follows:

$$F = \frac{1}{2} C_d \rho V(x, y, z, t)^2 A, \quad (6)$$

where  $C_d$  is the drag coefficient,  $\rho$  is the air density,  $V(x, y, z, t)$  is the transient wind velocity, and  $A$  is the effective area.

At any point in the structure, the transient wind velocity  $V(x, y, z, t)$  is the sum of the average wind velocity  $\bar{v}(z)$  and the pulse wind velocity  $v(x, y, z, t)$ .

$$V(x, y, z, t) = \bar{v}(z) + v(x, y, z, t). \quad (7)$$

The average wind velocity  $\bar{v}(z)$  varies with height. When the wind velocity at 10-m altitude is defined as the reference wind velocity,  $\bar{v}(z)$  varies exponentially with height.

$$\bar{v}(z) = v_{10} \left( \frac{z}{10} \right)^\alpha, \quad (8)$$

where  $v_{10}$  is the average wind velocity at the standard height (10 m),  $z$  is the altitude of the calculation point above ground, and  $\alpha$  is the ground roughness index.

The pulse wind velocity is simulated via a Gaussian stationary stochastic process with a zero average, the generation of which requires a theoretical or measured power spectral density function. In this paper, the Kaimal spectrum described<sup>30</sup> in EN61400-1 is used, defined as follows:

$$\frac{fS(f)}{\sigma^2} = \frac{4fL_k/V_{hub}}{(1 + 6fL_k/V_{hub})^{5/3}}, \quad (9)$$

where  $S(f)$  is the unilateral power spectrum of the pulse wind velocity,  $f$  is the frequency (Hz),  $L_k$  is the scale parameter of the wind velocity,  $\sigma$  is the standard deviation of the wind velocity, and  $V_{hub}$  is the average wind velocity at the hub.

The wind farm has spatial coherence, which is primarily represented as asynchrony of the wind direction and the wind velocity at each point in space. When the wind velocity at a point reaches the maximum level, at any point further away from this point, the wind velocity is less likely to reach this level. The pulse wind spatial correlation mainly includes left-right, top-bottom, and front-rear correlations. Therefore, for wind turbine tower, the pulse wind velocity spatial correlation coefficient for any two points  $i$  and  $j$  is as follows:

$$Coh_{ij}(f) = \exp \left\{ -12 \left[ (fr/V_{hub})^2 + (0.12r/L_c)^2 \right]^{0.5} \right\}, \quad (10)$$

where  $r$  is the spatial distance between two points  $i$  and  $j$  and  $L_c$  is the length scale parameter.

On the basis of Equation 9 and Equation 10, the cross-power spectral density function for any two points  $i$  and  $j$  at the wind turbine tower is as follows:

$$S_{ij}(f) = \sqrt{S_{ii}(f) \cdot S_{jj}(f) \cdot Coh_{ij}(f)}. \quad (11)$$

To simulate  $n$  wind velocity time-histories,  $n$  stationary Gaussian stochastic processes  $v_i(t) (i = 1, 2, \dots, n)$  with a zero average should be generated. The cross-spectral density matrix is as follows:

$$S(f) = [S_{ij}(f)]_{n \times n}. \quad (12)$$

$S(f)$  undergoes Cholesky decomposition to obtain the lower triangular matrix  $H(f)$ . The wind velocity time-history at the  $i$ th point is simulated based on following equation:

$$v_i(t) = \sum_{j=1}^i \sum_{k=1}^N |H_{ij}(\omega_k)| \sqrt{2\Delta\omega} \times \cos[\omega_k t - \theta_{ij}(\omega_k) + \varphi_{jk}] \quad (13)$$

where  $N$  is the number of frequency sampling points,  $\Delta\omega$  is the frequency spacing,  $\theta_{ij}(\omega_k) = \tan^{-1} \left[ \frac{\text{Im}H_{ij}(\omega_k)}{\text{Re}H_{ij}(\omega_k)} \right]$ , and  $\varphi_{jk}$  is the evenly distributed independent phase angle in the range of 0 to  $2\pi$ .

### 3.2 | Earthquake wave selection

In recent years, with the rapid growth of wind power, wind turbines are being constructed near faults and earthquake zones and wind turbine towers are vulnerable to near-field ground motion. The most notable feature of near-field ground motion is the directivity effect and the fling step effect induced by the pulsed ground motion. The most common form is a velocity pulse-like ground motion. Velocity pulse-like ground motion has a pulse-like waveform, a long pulse period, and rich medium/long period components. The ratio of the peak ground velocity (PGV) versus the peak ground acceleration (PGA) is large. Normally  $PGV/PGA \geq 0.2$ . As the wind turbine tower structure typically has a long period, near-field ground motion triggers an intense earthquake response or even leads to complete collapse.

In this paper, a near-field earthquake wave is selected using the following criteria. To ensure a pulse feature of the selected earthquake wave, the parameters are defined as follows:  $PGA > 100g$ ;  $PGV > 30cm/s$ ; pulse index<sup>31</sup>  $PI > 0.9$ ; and moment magnitude greater than 5.5. To investigate the effect of the pulse period on the structure's earthquake response, a near-field ground motion pulse period is selected in the range of 1.4 to 12.2 seconds. In total, 20 near-field earthquake waves that match the above criteria are selected (Appendix A.1). The selected earthquake waves are based on a previous study.<sup>31</sup> For comparison purposes, 20 ordinary far-field earthquake waves are selected as inputs (Appendix A.2). The selected far-field earthquake waves have the following parameters: fault distance greater than 50km and moment magnitude greater than or equal to 5.5.

## 4 | EXAMPLE ANALYSIS

### 4.1 | Model overview

In this study, the wind turbine hub height is 60 m. The tower is a cone with a thin shell, whose outer diameter declines linearly from 3.8 m at the base to 2.3 m at the top. The shell thickness along the entire height remains constant at 35 mm. The material parameters of the steel tower are listed in Table 1. The blade cross-section is a hollow rectangular section, with a height of 2 m, a width of 0.8 m, a length of 30 m, and a wall thickness of 15 mm. The blade elastic modulus is 65 GPa, the Poisson ratio is 0.2, and the density is  $2100 \text{ kg/m}^3$ . The cabin mass is 50 000 kg, and the hub mass is 20 000 kg. The spacing between the tower and the blade is 5 m.

The finite element model for this wind turbine tower was created using ABAQUS software. The cylindrical tower is simulated via thin shell element S4. The blade is simulated via elastic element Beam31. To model the interaction between the blade and the tower, the blade and tower are connected via a beam element with large stiffness. The cabin and hub are simulated via concentrated mass elements placed at the tower top and the blade connection center. The finite element model for the structure is shown in Figure 1.

To study the mesh convergence, two models (model 1 and model 2) with different element number are built for calculating the natural frequency. Model 1 has 5760 S4R shell elements and 204 B31 beam elements; model 2 has 57600 S4R shell elements and 2040 B31 beam elements. The vibration mode and natural frequency of the tower calculated by these two models are listed in Table 2. The calculating results of these two models are very similar. To save computing time, model 1 is chosen for the subsequent analysis. The first order frequency calculated by model 1 is also close to the first order frequency (0.57 Hz) calculated in Van der and Narasimhan's study.<sup>32</sup>

### 4.2 | Static pushover analysis

The nonlinear behavior of the tower structure is observed using a pushover analysis. On the basis of this, the tower structure failure performance is defined. In this paper, the displacement is increased gradually at the tower top along the front-rear direction via a displacement control method

**TABLE 1** The material parameters of the steel tower

$E$	$f_y$	$f_{yu}$	$\sigma_{lo}$	$C$	$\gamma$	$Q_\infty$	$b$	$\rho$
210 GPa	380 MPa	640 MPa	323 MPa	4200 MPa	26.5	317 MPa	6.6	7850 $\text{kg/m}^3$

**TABLE 2** Tower vibration mode and natural frequency [Colour table can be viewed at wileyonlinelibrary.com]

			
1st support structure side-to-side	1st support structure fore-aft	2nd support structure side-to-side	2nd support structure fore-aft
Model 1, $f = 0.54936$ Hz	$f = 0.55480$ Hz	$f = 2.8865$ Hz	$f = 3.2930$ Hz
Model 2, $f = 0.55693$ Hz	$f = 0.56298$ Hz	$f = 2.8944$ Hz	$f = 3.2995$ Hz

to obtain a variation curve of the base shear force versus top displacement (shown in Figure 4). The diagram also provides global and local deformation of the cylinder when the tower fails.

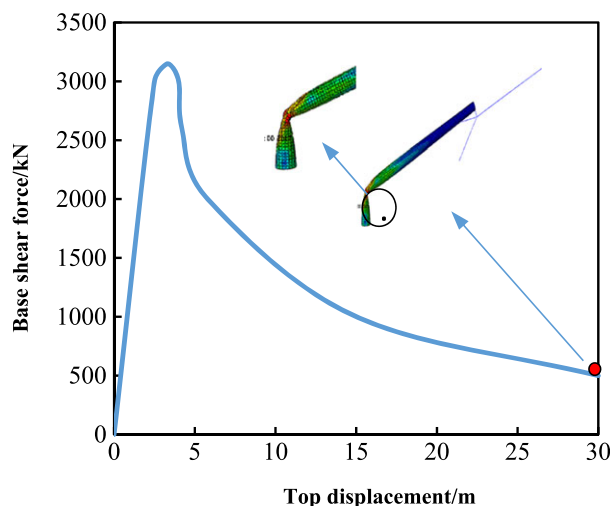
The diagram shows that when the top displacement is small, the base shear force changes linearly with top displacement, and the tower remains in the elastic phase. When the top displacement reaches 2 m, the tower base starts to yield. When the displacement reaches 3.8 m, the tower base yield reaches its maximum level, and the base shear force peaks at 3050 kN. After that, when the tower top displacement increases further, the base shear force decreases. The tower failure deformation diagram shows that the tower failure position is not at the tower base, but approximately 5 m above the tower base.

### 4.3 | Dynamic response analysis as a result of the coupled effects of wind and earthquake

This tower is located on a coastal wind farm. The wind velocity measurement data in this region show that the average wind velocity at a 10-m altitude in a typical year at the wind farm is 5.12 m/second; the maximum average wind velocity once in 50 years is 23.48 m/second; and the average turbulence intensity at each measurement height is approximately 0.173 to 0.128. A random wind velocity sample at different wind turbine positions is simulated using the method in Section 3.1. There are 30 points on the wind turbine blade and six points on the tower (Figure 5). Figure 6 shows the instantaneous wind velocity time-histories at the hub center (height = 60 m) and at a 7.5-m tower height.

A field earthquake risk analysis shows that this tower is in an earthquake prevention zone of degree 8 intensity. The acceleration peak of frequent earthquakes (50%, 50 y) is 0.11 g, and the acceleration peak of a rare earthquake (2%, 50 y) is 0.51 g.

First, the tower's dynamic response subject to a wind load is calculated. As a wind turbine normally stops during an earthquake, the time-history under a wind load is calculated via Equation 6 and imported into the ABAQUS model. The wind vibration response of a stopped wind turbine tower is calculated using the transient dynamic analysis module. In dynamic analysis, the tower damping matrix is based on Rayleigh damping, and the damping ratio is set<sup>33</sup> to 0.5%. The calculation shows that the mass damping coefficient is 0.213, and the stiffness damping coefficient is 0.004823. Figure 7 shows the tower top displacement time-history curves for an average annual wind velocity (red line) and a maximum wind velocity once in 50 years (black line). The diagram shows that for the two conditions, the maximum displacement values at the tower top are

**FIGURE 4** Tower static pushover curve [Colour figure can be viewed at wileyonlinelibrary.com]

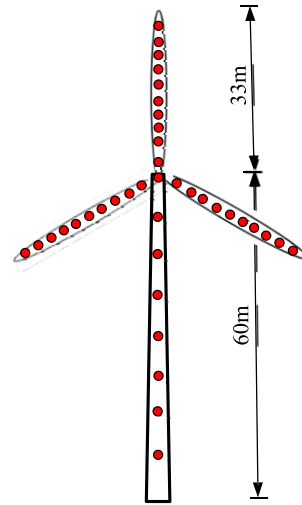


**FIGURE 5** Concentrated wind load point [Colour figure can be viewed at [wileyonlinelibrary.com](http://wileyonlinelibrary.com)]

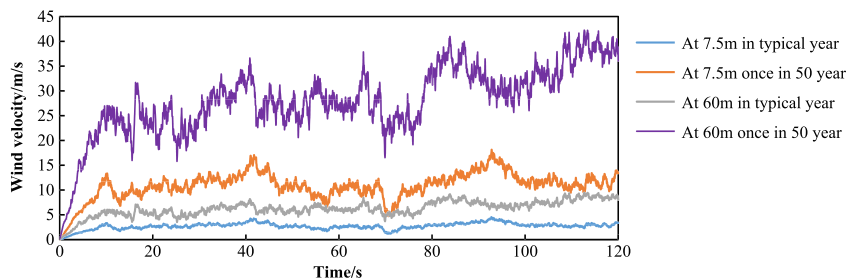


**FIGURE 6** Instantaneous wind velocity time-histories [Colour figure can be viewed at [wileyonlinelibrary.com](http://wileyonlinelibrary.com)]

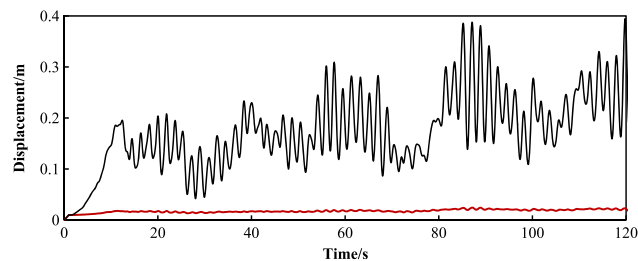


**FIGURE 7** Displacement time-history curves of tower top under wind load [Colour figure can be viewed at [wileyonlinelibrary.com](http://wileyonlinelibrary.com)]

0.028 and 0.39 m, which are significantly smaller than the 2-m displacement in the pushover analysis when the tower starts to yield. As the transient wind vibration response of the tower for the average annual wind velocity is at a low level, in the tower dynamic response analysis for the coupled effects of earthquake and wind, the average wind velocity is set to the maximum average wind velocity once in 50 years.

In Appendices A.1 and A.2, the PGA values of near-field and far-field earthquake waves are adjusted to 0.51 g, which are applied along the wind turbine tower front-rear horizontal direction after the wind load is applied for 60 seconds. Figure 8 shows the tower top displacement time-history curves for the 13th near-field earthquake wave in Appendix A.1 and the 14th far-field earthquake wave in Appendix A.2. Before

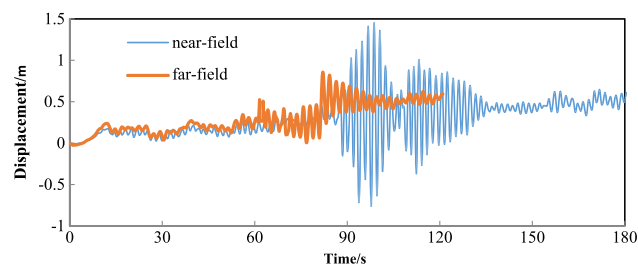


**FIGURE 8** Displacement time history curve of the top of tower under the coupling of wind and earthquakes [Colour figure can be viewed at [wileyonlinelibrary.com](http://wileyonlinelibrary.com)]

60 seconds, as there is only the wind load, the structure response is at a low level. After 60 seconds, because of the coupled effects of the earthquake and the wind, the structure response increases sharply. For a near-field wave, the displacement of the tower top reaches 1.45 m. For a far-field wave, the displacement at the tower top reaches 0.86 m.

To compare tower earthquake responses under far-field and near-field earthquake waves, Figure 9 shows the maximum tower deformation curves along the tower height for 20 near-field earthquake waves in Appendix A.1 and 20 far-field earthquake waves in Appendix A.2. The diagram shows that when the earthquake is a near-field pulse earthquake, the maximum tower displacement normally exceeds the value for a far-field earthquake. For a far-field earthquake, the average maximum displacement at the tower top is 0.7 m. For a near-field pulse earthquake, the average maximum displacement at the tower top is 0.95 m, which is 33.3% larger than the value for a far-field earthquake. However, both are smaller than the 2-m displacement associated with tower yielding in the pushover analysis. To investigate the effect of the near-field pulse period on the tower's earthquake response, Figure 10 shows the variation curve of the maximum displacement at the tower top versus the near-field pulse period. However, the diagram shows that the correlation between the maximum displacement at the tower top and the near-field pulse period is insignificant.

#### 4.4 | Collapse analysis subject to the coupled effects of wind and earthquake

In performance-based seismic evaluation of a structure, the structure's seismic collapse vulnerability is defined as conditional probability of structure collapse when subjected to an earthquake with a specific intensity. The governing mathematical expression is as follows:

$$F_R(im) = P(\text{Collapse} | IM = im), \quad (14)$$

where  $F_R(\cdot)$  is the structure collapse earthquake vulnerability function,  $P(\cdot)$  is the structure collapse probability, and  $IM$  is the ground motion intensity parameter, which is set to the peak ground acceleration (PGA) in this research.

Assuming that the structure collapse PGA follows a logarithmic normal distribution, then the probability of structure collapse under a specific PGA is calculated by the following equation:

$$F_R(PGA) = \Phi\left(\frac{\ln PGA - \hat{\mu}_{\ln PGA | \text{Collapse}}}{\hat{\beta}_{\ln PGA | \text{Collapse}}}\right), \quad (15)$$

where  $\Phi(\cdot)$  is the standard normal distribution function and  $\hat{\mu}_{\ln PGA | \text{Collapse}}$  and  $\hat{\beta}_{\ln PGA | \text{Collapse}}$  are the average and the standard deviations of  $\ln PGA_i$  when the structure collapses, which are calculated via following equations:

$$\hat{\mu}_{\ln PGA | \text{Collapse}} = \ln\left(\frac{\hat{\mu}_{PGA | \text{Collapse}}}{\sqrt{\delta^2 + 1}}\right) \quad \hat{\beta}_{\ln PGA | \text{Collapse}} = \sqrt{\ln(\delta^2 + 1)},$$

$$\hat{\mu}_{PGA | \text{Collapse}} = \frac{1}{n} \sum_{i=1}^n PGA_i \quad \hat{\beta}_{PGA | \text{Collapse}} = \frac{1}{n-1} \sum_{i=1}^n (PGA_i - \hat{\mu}_{PGA | \text{Collapse}})^2,$$

$$\delta = \hat{\beta}_{PGA | \text{Collapse}} / \hat{\mu}_{PGA | \text{Collapse}},$$

where  $PGA_i$  is the PGA when the structure collapses under the  $i$ th earthquake wave.

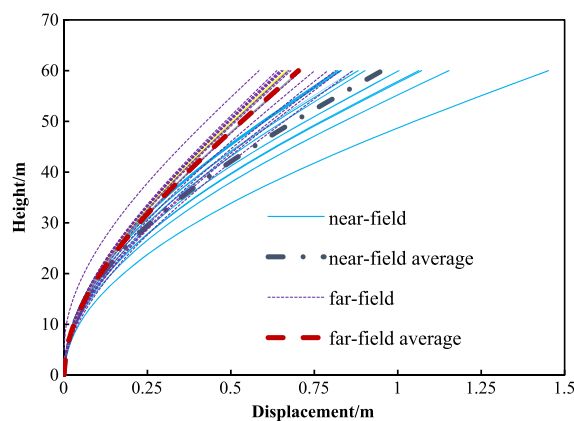


**FIGURE 9** Tower deformation along the tower height [Colour figure can be viewed at [wileyonlinelibrary.com](http://wileyonlinelibrary.com)]

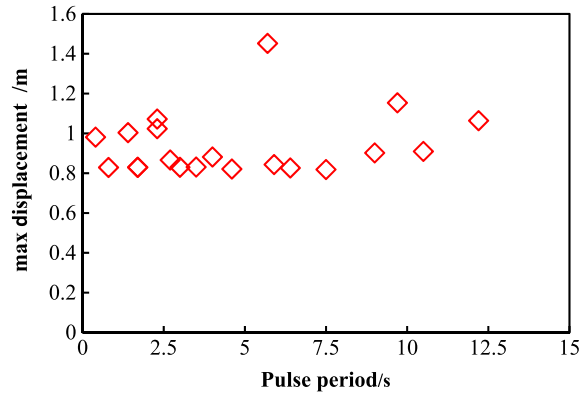


**FIGURE 10** The maximum displacement of the tower with the near-field pulse period changes [Colour figure can be viewed at wileyonlinelibrary.com]

The earthquake waves in Appendix A.1 and Appendix A.2 are used as inputs, and the coupled effects of the wind and the earthquake are considered. The *PGA* of each earthquake wave increases gradually until the wind turbine tower collapses (ie, the tower top displacement reaches 3.8 m). The *PGA* of each earthquake wave when the wind turbine tower collapses is shown in Figure 11.  $\hat{\mu}_{\ln PGA|Collapse}$  and  $\hat{\beta}_{\ln PGA|Collapse}$  are calculated from data in the diagram, which are substituted into Equation 15 to obtain the earthquake vulnerability curves for tower collapse failures for far-field and near-field earthquake waves (Figure 12). The diagram shows that the tower collapse probabilities under rare far-field and near-field earthquakes ( $PGA = 5.1 \text{ m/s}^2$ ) are low. When the collapse probability is 0.5, the near-field earthquake *PGA* is  $20 \text{ m/second}^2$ , and the far-field earthquake *PGA* is  $27 \text{ m/second}^2$ . This means that this tower has excellent seismic collapse resistance.

To further analyze the tower collapse pattern under intense earthquakes, the *PGA* values of four near-field pulse earthquake waves in Table 2 are increased to  $40 \text{ m/second}^2$  (with identical *PGA* values, the four earthquake waves generate a maximum displacement at the tower top). Figure 13 shows the tower top displacement time-history curve and the tower body global and local deformation curves under four near field pulse-like earthquake waves. The tower top maximum displacement has significantly exceeded the maximum displacement when the tower yields. At this moment, the tower collapses; the collapse position is always approximately 5 m above the tower base.

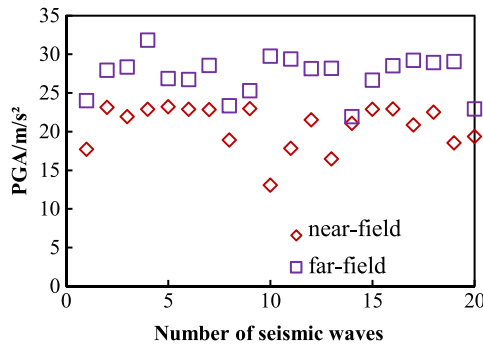


**FIGURE 11** *PGA* of each seismic wave when the wind tower collapse [Colour figure can be viewed at wileyonlinelibrary.com]

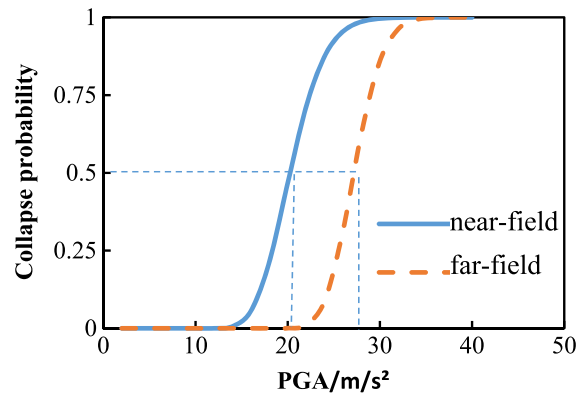


**FIGURE 12** Seismic vulnerability curve for turbine tower collapses [Colour figure can be viewed at wileyonlinelibrary.com]

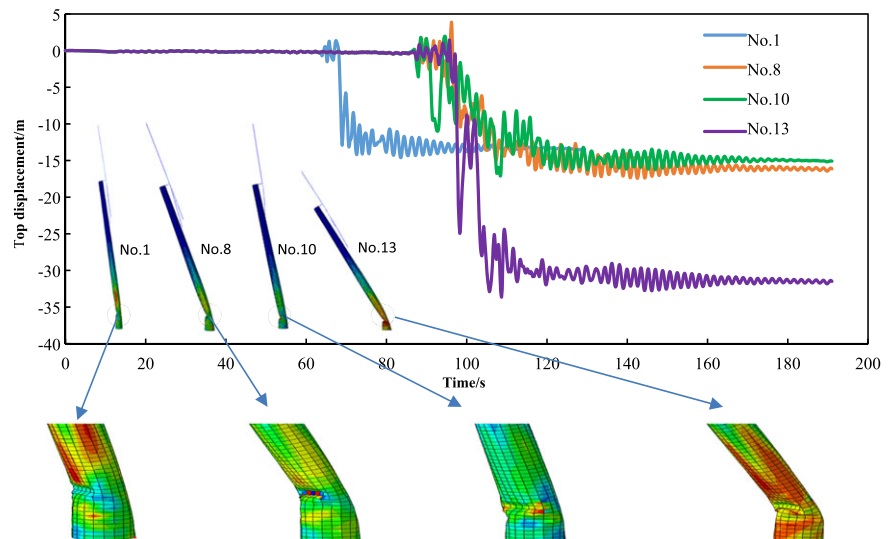


**FIGURE 13** Time-history of tower top displacement and global and local deformation of tower body under near-field impulsive seismic waves [Colour figure can be viewed at [wileyonlinelibrary.com](http://wileyonlinelibrary.com)]

## 5 | CONCLUSIONS

In this paper, the dynamic response of a wind turbine tower subject to the coupled effects of wind and a near-field intense earthquake is calculated using a nonlinear finite element method. A wind turbine tower with a 60-m high hub is used as an example for analysis. Near-field and far-field earthquake waves are selected as inputs. The seismic collapse vulnerability curve of this wind turbine tower is calculated. The tower seismic collapse capability and the seismic collapse pattern are analyzed. The following conclusions can be drawn:

1. A comparison with a static pushover test result for a small cylindrical tower proves that the nonlinear finite element model created in this paper can accurately simulate the tower stress pattern.
2. For the coupled effects of once-in-50-years wind loading and rare earthquakes, the displacement at the top of this tower is smaller than the yield displacement, and the tower remains in an elastic state. This means this tower has desirable antiseismic capability.
3. For a near-field earthquake wave, the average maximum tower displacement response is 33.3% larger than the value for a far-field earthquake wave. For velocity pulse near-field ground motion, the correlation between the maximum displacement at the tower top and the near-field pulse period is insignificant.
4. The seismic collapse vulnerability curve of this tower shows that under rare near-field and far-field earthquake waves, the probability of tower seismic collapse is small. When the collapse probability is 50%, the near-field earthquake wave PGA is 20 m/second<sup>2</sup>, and the far-field earthquake wave PGA is 27 m/second<sup>2</sup>. This means this tower has excellent seismic collapse resistance.
5. The dynamic seismic collapse pattern of this tower is similar to the static collapse pattern in the pushover analysis. Therefore, the static pushover analysis method is employed for tower seismic collapse capability evaluation.

## ORCID

Yanping Zhang  <http://orcid.org/0000-0003-4338-2697>

## REFERENCES

1. Bossanyi EA. *Bladed for Windows User Manual*. Bristol, UK: Garrad Hassan and Partners; 2000.
2. Jonkman JM, Jul MLJ. *FAST User's Guide*. EL 500e38230. National renewable energy Laboratory; 2005.
3. Witcher D. Seismic analysis of wind turbines in the time domain. *Wind Energy*. 2005;8(1):81-91.
4. Santangelo F, Failla G, Santini A, Arena F. Time-domain uncoupled analyses for seismic assessment of land-based wind turbines. *Eng Struct*. 2016;123:275-299.
5. Prowell I, Elgamal A, Uang C, Luco JE, Romanowitz H, Duggan E. Shake table testing and numerical simulation of a utility-scale wind turbine including operational effects. *Wind Energy*. 2014;17(7):997-1016.
6. Prowell I. An experimental and numerical study of wind turbine seismic behavior. PhD dissertation, University of California, San Diego; 2011.
7. Zhao X, Maiser P, Wu J. A new multibody modelling methodology for wind turbine structures using a cardanic joint beam element. *Renew Energy*. 2007;32(3):532-546.
8. Saravia CM, Machado SP, Cortinez VH. A composite beam finite element for multibody dynamics: application to large wind turbine modeling. *Eng Struct*. 2013;56:1164-1176.

9. Lee DL, Hodges DH, Patil MJ. Multi-flexible-body dynamic analysis of horizontal-axis wind turbines. *Wind Energy*. 2002;5(4):281-300.
10. Gebhardt CG, Preidikman S, Jørgensen MH, Massa JC. Non-linear aeroelastic behavior of large horizontal-axis wind turbines: a multibody system approach. *Int J Hydrogen Energy*. 2012;37(19):14719-14724.
11. Holm-Jørgensen K, Nielsen SRK. A component mode synthesis algorithm for multibody dynamics of wind turbines. *J Sound Vib*. 2009;326(3-5):753-767.
12. Holm-Jørgensen K, Nielsen SRK. System reduction in multibody dynamics of wind turbines. *Multibody Syst Dyn*. 2009;21(2):147-165.
13. Gebhardt CG, Rocca BA. Non-linear aeroelasticity: an approach to compute the response of three-blade large-scale horizontal-axis wind turbines. *Renew Energy*. 2014;66:495-514.
14. Bazeos N, Hatzigeorgiou GD, Hondros ID, Karamaneas H, Karabalis DL, Beskos DE. Static, seismic and stability analyses of a prototype wind turbine steel tower. *Eng Struct*. 2002;24(8):1015-1025.
15. Lavassas I, Nikolaidis G, Zervas P, Efthimiou E, Doudoumis IN, Baniotopoulos CC. Analysis and design of the prototype of a steel 1-MW wind turbine tower. *Eng Struct*. 2003;25(8):1097-1106.
16. Nuta E, Christopoulos C, Packer JA. Methodology for seismic risk assessment for tubular steel wind turbine towers: application to Canadian seismic environment. *Can J Civ Eng*. 2011;38(3):293-304.
17. Asareh MA, Schonberg W, Volz J. Effects of seismic and aerodynamic load interaction on structural dynamic response of multi-megawatt utility scale horizontal axis wind turbines. *Renew Energy*. 2016;86:49-58.
18. Asareh M.A., Volz JS. Evaluation of aerodynamic and seismic coupling for wind turbines using finite element approach, in: ASME 2013 International Mechanical Engineering Congress and Exposition: American Society of Mechanical Engineers. 2013, pp. V04BT04A041-004BT004A041.
19. Asareh MA, Schonberg W, Volz J. Fragility analysis of a 5-MWNREL wind turbine considering aero-elastic and seismic interaction using finite element method. *Finite Elements in Analysis and Design*. 2016;120:57-67.
20. Patil A, Jung S, Kwon OS. Structural performance of a parked wind turbine tower subjected to strong ground motions. *Eng Struct*. 2016;120:92-102.
21. Kim DH, Lee SG, Lee IK. Seismic fragility analysis of 5MW off shore wind turbine. *Renew Energy*. 2014;65:250-256.
22. Mo RJ, Kang HG, Li M, Zhao XL. Seismic fragility analysis of monopile offshore wind turbines under different operational conditions. *Energies*. 2017;10(7):1037.
23. Champion C, Liel A. The effect of near-fault directivity on building seismic collapse risk. *Earthq Eng Struct Dynam*. 2012;41(10):1391-1409.
24. Kalkan E, Kunnath S. Effects of fling step and forward directivity on seismic response of buildings. *Earthq Spectra*. 2006;22(2):367-390.
25. Alavi B, Krawinkler H. Behavior of moment-resisting frame structures subjected to near-fault ground motions. *Earthq Eng Struct Dynam*. 2004;33(6):687-706.
26. Stamatopoulos G. Response of a wind turbine tower subjected to near-fault excitation and comparison with the Greek aseismic code provisions. *Soil Dyn Earthq Eng*. 2013;46:77-84.
27. Sadowski AJ, Camara A, Málaga-Chuquitaype C, Dai K. Seismic analysis of a tall metal wind turbine support tower with realistic geometric imperfections. *Earthquake Engineering and Structural Dynamics*. 2017;46(2):201-219.
28. Katsanos EI, Thons S, Georgakis CT. Wind turbines and seismic hazard: a state-of-the-art review. *Wind Energy*. 2016;19(11):2113-2133.
29. Sim HB, Prowell I, Elgamal A, Uang CM. Flexural tests and associated study of a full-scale 65-kW wind turbine tower. *J Struct Eng*. 2014;140(5):04013110.
30. IEC61400-1 Ed.3. Wind turbines-part 1: design requirements, Inter-national Electro technical Commission, Geneva, Switzerland, 2005.
31. Baker J. Quantitative classification of near-fault ground motions using wavelet analysis. *Bull Seismol Soc Am*. 2007;97(5):1486-1501.
32. Van der Woude C, Narasimhan S. A study on vibration isolation for wind turbine structures. *Eng Struct*. 2014;60:223-234.
33. Valamanesh V, Myers A. Aerodynamic damping and seismic response of horizontal axis wind turbine towers. *J. Struct. Eng*. 2014;140(11):04014090.

**How to cite this article:** Fan J, Li Q, Zhang Y. Collapse analysis of wind turbine tower under the coupled effects of wind and near-field earthquake. *Wind Energy*. 2018;1-13. <https://doi.org/10.1002/we.2294>

## APPENDIX A

## NEAR-FIELD EARTHQUAKE WAVES

No.	Name of near-field earthquake wave	$M_w$	D (km)	$T_p$ (s)	PGV(m/s)	PGA(m/s <sup>2</sup> )	PGV/PGA	PI
1	Imperial Valley-06, 1979, Agrarias	6.5	2.6	2.3	0.544	1.9	0.29	1.0
2	Imperial Valley-06 1979, El Centro Array #4	6.5	27.1	4.6	0.779	3.9	0.20	1.0
3	Erzincan, Turkey, 1992, Erzincan	6.7	9.0	2.7	0.954	2.2	0.43	1.0
4	Cape Mendocino, 1992, Petrolia	7.0	4.5	3.0	0.821	0.7	1.17	0.92
5	Landers, 1992, Yermo Fire Station	7.3	86.0	7.5	0.532	1.4	0.38	1.0
6	Northridge-01, 1994, LA Dam	6.7	11.8	1.7	0.771	1.3	0.59	1.0
7	Northridge-01,1994,Sylmar—Converter Sta	6.7	13.1	3.5	1.303	2.7	0.48	0.92
8	Chi-Chi, Taiwan, 1999, CHY035	7.6	43.9	1.4	0.42	1.5	0.28	0.95
9	Chi-Chi, Taiwan, 1999, TCU029	7.6	79.2	6.4	0.623	3.9	0.16	1.0
10	Chi-Chi, Taiwan, 1999, TCU065	7.6	26.7	5.7	1.277	4.5	0.28	0.96
11	Chi-Chi, Taiwan, 1999, TCU068	7.6	47.9	12.2	1.911	9.4	0.20	1.0
12	Chi-Chi, Taiwan, 1999, TCU076	7.6	16	4.0	0.637	3.5	0.18	0.92
13	Chi-Chi, Taiwan, 1999, TCU102	7.6	45.6	9.7	1.066	2.5	0.43	0.97
14	Chi-Chi, Taiwan, 1999, TCU128	7.6	63.3	9.0	0.787	4.7	0.17	1.0
15	Loma Prieta, 1989, Gilroy Array #2	6.9	29.8	1.7	0.457	1.5	0.30	0.98
16	Whittier Narrows-01 1987 Downey—Co Maint Bldg	6.0	16.0	0.8	0.304	0.7	0.43	1.0
17	Chi-Chi, Taiwan, 1999, TCU054	7.6	37.6	10.5	0.609	6.9	0.09	1.0
18	Kocaeli, Turkey, 1999, Gebze	7.5	47.0	5.9	0.52	4.2	0.12	1.0
19	Superstition Hills-02 1987, Parachute Test Site	6.5	16.0	2.3	1.068	1.9	0.56	1.0
20	Coalinga-07, 1983, Coalinga-14th & Elm (Old CHP)	5.2	9.6	0.4	0.361	0.3	1.20	1.0

## APPENDIX B

## FAR-FIELD EARTHQUAKE WAVES

No.	Name of far-field earthquake wave	$M_w$	PGA(m/s <sup>2</sup> )
1	Imp.Vall. 1979, El Centro ARRAY#13	6.5	1.394
2	Imp.Vall. 1979, Chihuahua	6.5	2.704
3	Imp.Vall. 1979, Computertas	6.5	1.862
4	Imp.Vall. 1979, Westorela,Fire	6.5	1.086
5	Loma Pr. 1989, Agnew State Hosptial	6.9	1.730
6	Loma Pr. 1989, Coyote Lake Dam	6.9	1.791
7	Loma Pr. 1989, WAHO	6.9	6.718
8	Loma Pr. 1989, Anderson Daw Downstrm	6.9	2.439
9	Loma Pr. 1989, Hollister Diff Array	6.9	2.785
10	Loma Pr. 1989, Sunnyvale Colton Ave	6.9	2.082
11	Northridge. 1994, LA Holly wood storage	6.7	3.582
12	Northridge. 1994, Glendale Las Palmas	6.7	3.570
13	Northridge. 1994, La obregon Park	6.7	5.625
14	Northridge. 1994, Canoga Park Topange	6.7	4.200
15	Northridge. 1994, La Cypress Ave	6.7	2.103
16	Northridge. 1994, La Univ. Hospital	6.7	4.930
17	Loma Pr. 1989, Gilroy Array#4	6.9	4.170
18	Loma Pr. 1989, Gilroy Array#7	6.9	3.230
19	Superstition Hills. 1987, Parechute Test site	6.7	4.550
20	Superstition Hills. 1987, El Centro Imp. Co. Cent	6.7	3.580